PMS-Net: Robust Haze Removal Based on Patch Map for Single Images

Wei-Ting Chen [1] Jian-Jiun Ding [2] Sy-Yen Kuo [2]

[1] Graduate Institute of Electronics Engineering, National Taiwan University, Taipei 106, Taiwan
[2]Department of Electrical Engineering, National Taiwan University, Taipei 106, Taiwan

{r05943089, jjding, sykuo}@ntu.edu.tw

Abstract

In this paper, a novel haze removal algorithm based on a new feature called the patch map is proposed. Conventional patch-based haze removal algorithms (e.g. the dark channel prior) usually performs dehazing with a fixed patch size. However, it may lead to several problems such as oversaturation and color distortion. Therefore, in this paper, we designed an adaptive and automatic patch size selection model called the Patch Map Selection Network (PMS-Net) to select the patch size corresponding to each pixel. This network is designed based on the convolutional neural network (CNN), which can generate the patch map from the input image. Experimental results on both synthesized and real-world hazy images show that, with the combination of the proposed PMS-Net, the performance in haze removal is much better than that of state-of-the-art algorithms and we can address the problems caused by the fixed patch size.

1. Introduction

Haze is an atmospheric phenomenon which compose of smoke, dust and other floating particles. They may degrade the visibility and lead to the poor performance of image processing such as object detection and classification. Narasimhan *et al*. [1] modeled the hazy scene as:

$$I(x) = J(x)t(x) + A\left(1 - t(x)\right) \tag{1}$$

where $J(x)$ is the haze-free image, $I(x)$ is the observed hazy image, A is the global atmospheric light which indicates the luminance of the light source from infinite distance away, and $t(x)$ is the transmission map which can be denoted as $t(x)=e^{-\beta d(x)}$, where β is the scattering coefficient and $d(x)$ is the path length. We can rewrite (1) as:

$$J(x) = \frac{I(x) - A}{t(x)} + A. \tag{2}$$

Then, one can notice that, to get better recovered results in haze removal, the critical parameters are $t(x)$ and A.

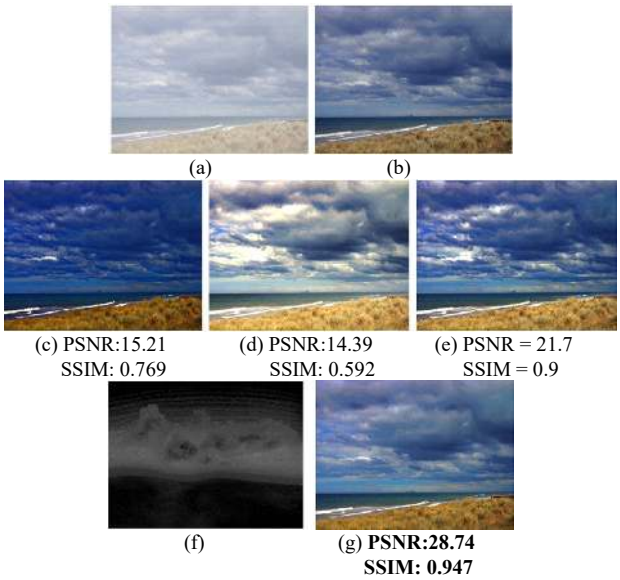

Figure 1: Dehazing results of the proposed patch map compare to the method with fixed patch size. (a) Input image; (b) the ground truth; (c)-(e) recovered by the fixed patch sizes of 1, 120, 15; (f) the patch map determined by the proposed algorithm; (g) recovered image by the patch map.

There have been many algorithms [2-22] addressing the image dehazing problem. Tarel *et al*. [2] applied the special bilateral filter to investigate the atmospheric veil. He *et al*. [4] proposed the dark channel prior (DCP) based on the statistical results of natural haze-free images to compute the transmission map. In [14], Tang *et al*. applied machine learning techniques to predict the transmission map. In recent years, several deep-learning based dehazing methods [15-22], including the DehazeNet [15], the multi-scale CNN (MSCNN) [16], the residue learning technique [18], the quad-tree CNN [19], and the densely connected pyramid dehazing network [21], were proposed for haze removal. For haze removal in the night time case, various algorithms [23-27] were proposed to solve this problem.

Although there have been many dehazing algorithms, there are still several limitations that constrain the performance of recovered results. Traditional algorithms

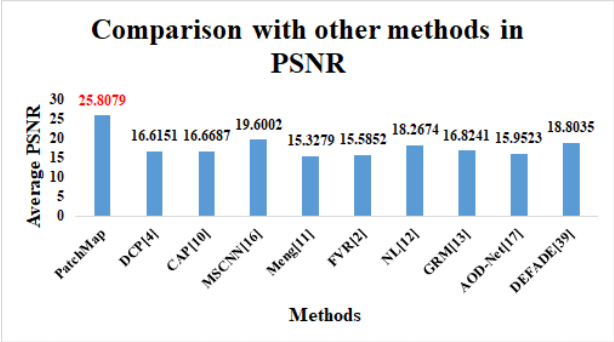

(a)

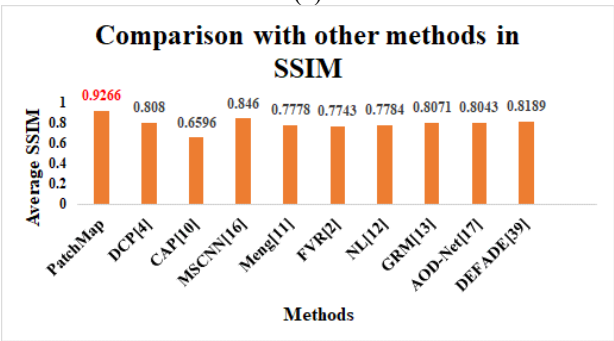

(b)

Figure 2: Comparing the performance with state-of-the-art algorithms by using the patch map based DCP.

are usually based on the prior related to human perception. However, these priors may be invalid in some scenarios. For example, the DCP may have limited performance in sky regions or white scenarios because the transmission map cannot be well predicted in these cases. On the other hand, for the learning-based methods, without using human- selected features, the transmission map may not be predicted accurately in general since they may bound the mapping space with less haze-relevant features.

In this paper, inspired by the DCP, we proposed a novel algorithm based on the new feature called the patch map, which can select the patch size adaptively for each pixel. In the traditional DCP algorithm, a fixed patch size is applied to estimate the atmospheric light and the transmission map. However, from Fig. 1, one can see that when we perform the DCP with the fixed-size patch (in this figure, we use 1, 15, and 120) to recover the hazy scene, the performance is limited. However, when we apply the patch map to estimate the dark channel with the adaptive patch size, the performance of the DCP can be effectively enhanced. In Fig. 2, we use the SOTS dataset in [30] to compare the performance of the patch map-based DCP with other algorithms. From Fig. 2, one can see that the performance of the traditional DCP with the fixed patch size is not better than that of other state of the art algorithms. Nevertheless, when we applied the patch map to choose the patch size in each pixel, the performance become the best among all algorithms. From this analysis, we can conclude that, with the use of the proposed patch map, the performance of the DCP can be effectively improved.

Therefore, in this article, **first**, we analyze the reasons why the DCP is invalid in the certain scenarios and why using a fixed patch size will lead to the bad performance. **Second**, we define a new feature named the patch map to address this problem. **Third**, we proposed the patch map selection network (**PMS-Net**) to generate the patch map. In order to enhance the performance of this network, the Multiscale U-module with pyramid style is proposed. Then, with the patch map, the more precise atmospheric light and the transmission map can be predicted. With the proposed architecture, the problems of the traditional DCP can be avoided (e.g. the error recovery in white or bright scenes) and the quality of the recovered images is higher than that of other algorithms. **Last**, we analyze the properties of the patch map and conclude the rule of selecting the patch size in the DCP. To the best of our knowledge, this is the first work to perform the CNNs for patch map generation to remove haze. Simulations show that, compared to other existing algorithms, the proposed method has the best performance in both the synthetic dataset and the real world images.

This article is organized as follows. In Section 2, we will review several related works. In Section 3, the detailed procedure of our proposed algorithm will be demonstrated. In Section 4, the experimental results compared to other state of the art haze removal algorithms are provided. In Section 5, a conclusion is given.

2. Related Works

2.1. Dark Channel Prior

From statistical analysis, He *et al.* [4] found that the dark channels of natural haze-free images are close to zero:

$$J_{Dark}(x) = \min_{k\in\{r,g,b\}}\left(\min_{y\in\Omega(x)} J^k(x)\right) \cong 0. \tag{3}$$

where $J^k(x)$ is one of the color channel in the haze-free image and $\Omega(x)$ is a local patch centered at x. We call (3) the dark channel prior (DCP). According to the DCP, we can reformulate (1) as:

$$\min_{y\in\Omega(x)}\left(\min_{k\in\{r,g,b\}}\frac{I^k(y)}{A^k}\right) = \min_{y\in\Omega(x)}\left(\min_{k\in\{r,g,b\}}\frac{J^k(y)}{A^k}\right)t(x)+1-t(x)$$
$$\cong 1-t(x). \tag{4}$$

Then, we can estimate the transmission map from:

$$t(x) = 1-\omega\min_{y\in\Omega(x)}\left(\min_{k\in\{r,g,b\}}\frac{I^k(y)}{A^k}\right) \tag{5}$$

where ω is a constant. With the estimation of the transmission map, the haze-free results can be recovered.

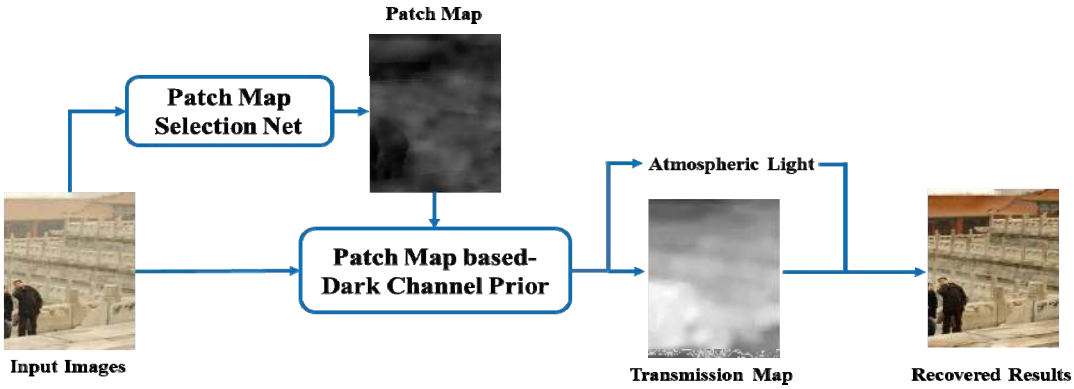

Figure 3: The flowchart of the proposed haze removal algorithm.

Although this method is powerful, it may be invalid in some scenarios, which lead to some problems such as oversaturation and underestimation of the transmission maps. From our analysis, the patch size selection for each hazy pixel may affect the recovered result a lot. Thus, instead of using a fixed patch size, we propose a network to learn the proper patch size automatically and adaptively for each hazy pixel.

2.2. Traditional Algorithms for Haze Removal

In addition to the DCP method [4], Tarel *et al*. [2] applied the bilateral filter and white balanced technique and Tan *et al*. [3] adopted the Markov random field to cope with the haze problem. Fattal *et al*. [5, 6] estimated the albedo of the scene and used the color-line concept to recover hazy images. Ancuti *et al*. [7-9] used the semi-inverse image method and the fusion method to perform dehazing. Zhu *et al*. [10] proposed a color attenuation prior based dehazing method. Meng *et al*. [11] applied the boundary constraint derived from the haze model and Berman *et al*. [12] proposed a non-local image dehazing method. Chen *et al*. [13] proposed the Gradient Residual Minimization (GRM) recover the hazy scene and minimize the visual artifacts.

2.3. Learning-Based Haze Removal

Recently, many haze and smoke removal algorithms based on learning techniques have been proposed. Tang *et al*. [14] used the random forest regression [29] to predict the transmission map by extracting several haze-relevant features (e.g. the dark channel, saturation, contrast, and the hue disparity). They found that the dark channel is the most dominant feature while predicting the transmission map.

For deep learning based methods, Cai *et al*. [15] built an end to end CNN-based haze removal system, which is called the DehazeNet to predict the transmission map of hazy images. Ren *et al*. [16] developed the multi-scale CNN (MSCNN) composed of the coarse-scale and the fine-scale networks. Moreover, instead of computing the transmission map and the atmospheric light value separately, Li *et al*. [17] combined these two variables. Yang *et al*. [20] proposed the proximal dehaze-net, which combined the haze model, the dark channel, and the transmission prior by using the energy function. Zhang *et al*. [21] developed the densely connected pyramid dehazing Network (DCPDN) to evaluate the transmission map, the atmospheric light, and the dehazed image jointly. For smoke removal, Chen *et al*. [28] proposed a novel model based on the random forest regression [29] and channel-based smoke removal.

3. Proposed Method

In this section, we illustrate the details of the proposed dehazing algorithm and the flow chart is shown in Fig. 3.

3.1. Wrong Recovery in the Dark Channel Prior

Although the conventional DCP is powerful and can deal with the hazy scenario effectively, it usually leads to some problems, including the oversaturation problem and the color distortion in white scenes or ordinary scenes. (see Fig. 8) The reasons causing these problems are as follows. In the original assumption, the minimum of three color channels in the local patch is close to zero for haze-free images. Then, with this prior, (4) can be reduced to (6).

$$t(x) = 1 - \min_{y \in \Omega(x)} \left(\min_{k \in \{r,g,b\}} \frac{I^k(y)}{A^k} \right). \tag{6}$$

However, this reduction is the main reason causing the problems mentioned above since conventionally one usually set a fixed patch size. If a small or a medium patch size such as 5 or 15 is chosen, the value of the dark channel may not always be zero, especially for the regions with larger intensity (see the examples in Fig. 6).

Eq. (6) is derived based on the assumption that the dark channel is near to zero. If the patch size is small, the assumption will fail and (6) may be invalid. In this case, instead of (6), the transmission map $t(x)$ is formulated as

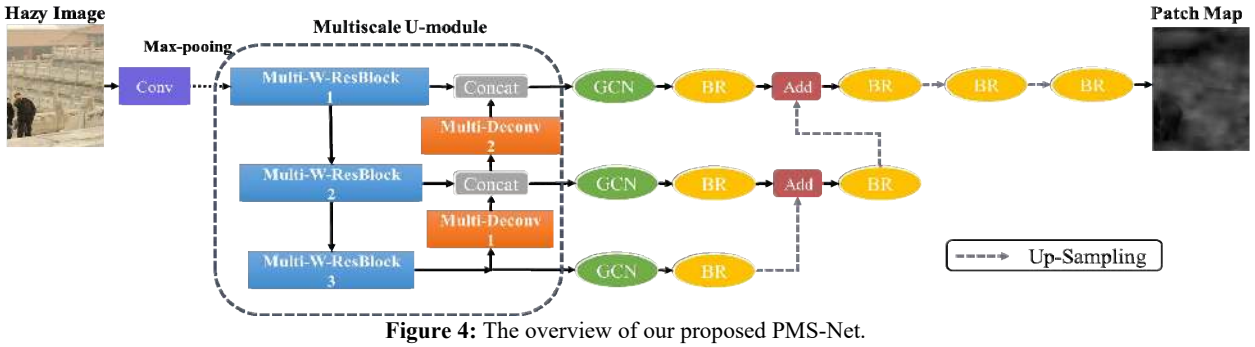

Figure 4: The overview of our proposed PMS-Net.

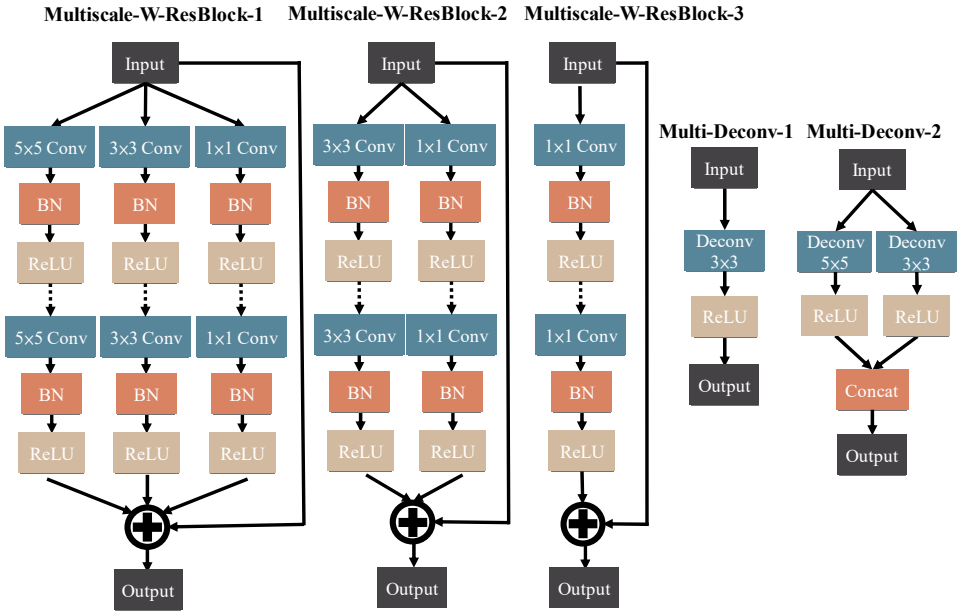

Figure 5: The structure of the proposed Multi-W-ResBlock and the Multi-Deconv block.

Figure 6: White scenes may have the dark channel far from zero. (1st column is the input; 2nd and 3rd is the dark channel estimated by the patch size 15 and 120).

$$t(x)=\frac{1-\min\limits_{y\in\Omega(x)}\left(\min\limits_{k\in\{r,g,b\}}\frac{I^k(y)}{A^k}\right)}{1-\min\limits_{y\in\Omega(x)}\left(\min\limits_{k\in\{r,g,b\}}\frac{J^k(y)}{A^k}\right)}. \qquad (7)$$

However, since $J^k(y)$ is usually unable to know, the transmission map cannot be determined from (7). Note that $t(x)$ determined from (6) will be smaller than that determined from (7) since the denominator in (7) is less than 1. Therefore, using (6) may underestimate the transmission map if the patch is fixed to a small size, especially for the regions with white and bright color.

By contrast, if the patch size is fixed to a large size, although the dark channel is usually near to zero, the halo artifacts [4] is caused and the computation is increased. As a result, selecting the patch size adaptively for each pixel is crucial to get high quality recovered results.

Therefore, we propose the Patch Map Selection Network (PMS-Net) to select the patch size adaptively. Its architecture is shown as in Fig. 4.

Figure 7: The patch map generated by the method in sub-section 3.2. (The upper row: input hazy images; The lower row: corresponding patch maps)

3.2. Patch Map Generator

To train the PMS-Net, we need to generate the patch map from the training data. Thus, we propose the patch map generator (PMG).

The design of the PMG is that, initially, we apply (8) and (9) to recover the image with different patch sizes.

$$t_i(x) = 1 - \omega \min_{y \in \Omega_i(x)} \left(\min_{k \in \{r,g,b\}} \frac{I^k(y)}{A_i^k(y)} \right), \; i = 1,...,n \tag{8}$$

$$J_i(x) = \frac{I(x) - A_i^k}{t_i(x)} + A_i^k, \; k \in \{r,g,b\} \; i = 1,...,n \tag{9}$$

where $I(x)$ is the input, $t_i(x), J_i(x), A_i^k(x)$ are the transmission maps, the haze-free images and the atmospheric light values with different patch sizes i, respectively. Then, we calculate the error function between the recovered results and the ground truth by:

$$E_i(x) = \left| J_{gth}(x) - J_i(x) \right|, \; i = 1,...,n \tag{10}$$

where $E_i(x)$ is the error function of the recovered result with patch size i and $J_{gth}(x)$ is the ground truth. We determine the error functions for different patch sizes i and find the patch size with the lowest error function for each pixel and assign it as the patch map value of the pixel:

$$PMG(x) = k, \; \forall k \quad s.t \quad E_k(x) = \min\left(E_i(x)\right), i = 1,...,n \tag{11}$$

where $PMG(x)$ is the patch map and k is the patch size that can minimize the error function at the location x. In this case, we set the n as 120. With this operation, we can produce the patch map for all images and use them for the training procedure.

The examples of patch map are shown in Fig. 7. One can see that, in the white, gray, bright, and sky region, the patch size prefers to be higher in order to fit the dark channel prior. (see the sky and white region) Otherwise, in the other dark region, the patch size is preferred to be small.

3.3. Patch Map Selection Net

The structure of the proposed PMS-Net is shown in Fig. 4. It can be divided into the encoder part and the decoder part. Originally, the input hazy image will be projected to the higher dimension space by convolving a 3×3 kernel with 16 filters. Then, the proposed Multiscale U-module is applied to extract the features from this higher dimension data.

The design of the multiscale U-module is shown in Fig. 4. The input will pass several Multiscale–W-ResBlocks (MSWR) which are shown in the left side of Fig. 5. For the design of the MSWR, inspired by the Wide-ResNet (WRN) [31], which improves the ResNet [32] by increasing the width and decrease the depth of the network, we apply the WRN in our network. In each block, we perform the *Conv-BN-ReLu-Dropout-Conv-BN-ReLu* with a shortcut to extract the information. Moreover, the design of the multi-scale concept in the MSWR is inspired by Inception-ResNet [42] and [9, 14, 15, 16, 17, 21] which adopted the multi-level technique to enhance the variety of the information and extract the detailed information. By this operation, the network can find the transmission map or the haze-free image more effectively. Although in this network, the output is different from previous works, we still apply this technique because we believed that the patch map is the haze-related feature.

Besides, instead of using the same architecture of the MSWR, the pyramid style is performed in order to extract the information in different level. More specifically, for the first block, we connect three convolutional kernels with various sizes (5×5, 3×3, 1×1) because we need to preserve more information in different scale in the higher layer. For the second and the third blocks, the convolutional kernels with (3×3, 1×1) and (1×1) are adopted respectively. By this operation, the use of parameters can be reduced as well.

For the other part in the Multiscale U-module, we use the Multi-Deconv module to concatenate the information with the output of the MSWR instead of the traditional deconvolution, since the deconvolution layer can help the network to reconstruct shape information of the input data [33]. Therefore, with the combination of the multiscale deconvolution, we can reconstruct more precise feature maps from the previous layers. In addition, in the design of the Multi-Deconv, we also performed the pyramid style to up-scale the information to concatenate with MSWR. The reason is the same as the design of the MSWR. That is, the feature maps in the different levels should be deconvolved with various scale (see the right side in Fig. 5)

To preserve the high resolution features, the outputs of the MSWR and the Multi-Deconv module are concatenated directly. Then, the feature maps will be fed into the Multi-Deconv in the higher layers and the decoder. For the design of the decoder, we adopt the global

Table 1: Qualitative analysis on the **Test A** dataset.

	CAP [10]	MSCNN [16]	AOD-Net [17]	NL [12]	FVR [2]	GRM [13]	Meng [11]	DEFADE [39-41]	DCP [4]	Ours
MSE	0.0509	0.0627	0.0703	0.0526	0.0441	0.0398	0.0246	0.0604	0.0249	**0.0139**
SSIM	0.6906	0.7028	0.7115	0.6635	0.6915	0.7863	0.7749	0.6435	0.8234	**0.8684**
PSNR	13.735	12.7597	12.396	13.3394	14.24	14.862	16.4119	12.7167	16.553	**19.2121**
CIEDE2000	13.331	15.8265	16.063	15.3333	15.045	11.381	10.1913	16.4385	8.9547	**6.0652**

Table 2: Qualitative analysis on the **Test B** dataset.

	CAP [10]	MSCNN [16]	AOD-Net [17]	NL [12]	FVR [2]	GRM [13]	Meng [11]	DEFADE [39-41]	DCP [4]	Ours
MSE	0.0363	0.02083	0.0264	0.02833	0.0283	0.0315	0.0342	0.03693	0.0307	**0.0139**
SSIM	0.6838	0.85407	0.8644	0.74903	0.7944	0.8088	0.7859	0.7428	0.8131	**0.8775**
PSNR	14.973	18.3836	17.244	16.8172	15.999	16.293	15.564	15.7237	16.568	**20.152**
CIEDE2000	13.275	9.04877	10.282	11.8897	12.402	11.822	12.7754	13.949	11.351	**7.2965**

Table 3: Quantitative MSE evaluation for ablation study on the set of **Test A+B**

	Module A	Module B	Module C
MSE	0.04415	0.0398	**0.03635**

convolutional network modules (GCN) [34]. The boundary refinement module (BR) [34] is also applied to preserve the edge information. For the up-scale layer, the up-sampling operation is adopted. Furthermore, the densely connected style [35, 36] is applied to merge the high-resolution and the low-resolution information. With the proposed PMS-Net, the patch map can be predicted well.

4. Experimental Results

In this section, we will demonstrate the performance of our proposed haze removal algorithm. We will adopt two different state-of-the-art synthetic haze datasets and one real world hazy image dataset to compare the performance.

4.1 Datasets and the Training Implementation

In this work, we adopt the NYU-depth2 dataset [37] and the RESIDE dataset [30]. In the training procedure, we use 2192 images in total which consists of 1200 images from the NYU-depth2 dataset, 492 images from the RESIDE dataset, and 500 synthesized images as our training data. In the training model, the learning rate is e^{-4} and the Adam optimizer [38] is adopted. The batch size is set to 4 and the loss function is the mean square error (MSE). In each epoch, we adopt early stopping and use the 10 % of the original data as the validation set. Similar to other works of dehazing, for the test dataset, we use the remained images in these datasets as the test set. We ensure that none of these test images was used in the training process. We take 150 images from the NYU-depth2 dataset and apply synthesized haze on these images as **Test A**. Then, we take 200 outdoor images and 100 indoor images from RESIDE dataset and NYU-depth2 dataset as **Test B**.

4.2 Qualitative Comparison on Synthetic Data

We apply four assessment metrics: the mean square error (MSE), the structural similarity (SSIM), the peak-to-peak signal to noise ratio (PSNR), and the CIEDE2000 color difference. Then, we perform nine existing dehazing algorithms which are the **DCP** [4] (CVPR' 09), the **CAP** [10] (TIP' 15), the **MSCNN** [16] (ECCV' 16), the **NL** [12] (CVPR' 16), the **Meng** [11] (ICCV, 13), the **FVR** [2] (CVPR' 09), the **GRM** [13] (ECCV' 16), the **DEFADE** [39-41] (TIP' 15), and the **AOD-Net** [17] (ICCV' 17).

The comparison results are shown in Table 1 and Table 2. One can find that our proposed method has the best performance in haze removal in all metrics comparing to other methods in both two test datasets. Note that the proposed method has high fidelity for color preservation since it has much lower values of the CIEDE2000 color difference than other methods. Furthermore, comparing to the conventional DCP, with the fixed patch size, the performance of proposed method is much better (the MSE is **49%** less, the SSIM is increased by **6%**, the PSNR is **19%** higher, and the CIEDE2000 color difference is **34%** less). Thus, our proposed method can enhance the performance of the conventional DCP effectively.

4.3 Dehazed Results in Real World Images

We demonstrate the improvement of the proposed method by comparing the recovered images with other methods visually in Fig. 8. We adopt the images which were also used as the test data in previous works.

From Fig. 8, one can see that our proposed method can well remove the haze from images without hurting the image quality (see the 1st (waterfall), 3rd (mountain), 5th (stadium), 6th (girls)). Moreover, with the proposed method, the color shift problem and the oversaturation problem can be well avoided. Especially, one can observe that our proposed algorithm can prevent losing the color fidelity in the white hazy scenes (see the pictures in the 1st(waterfall),

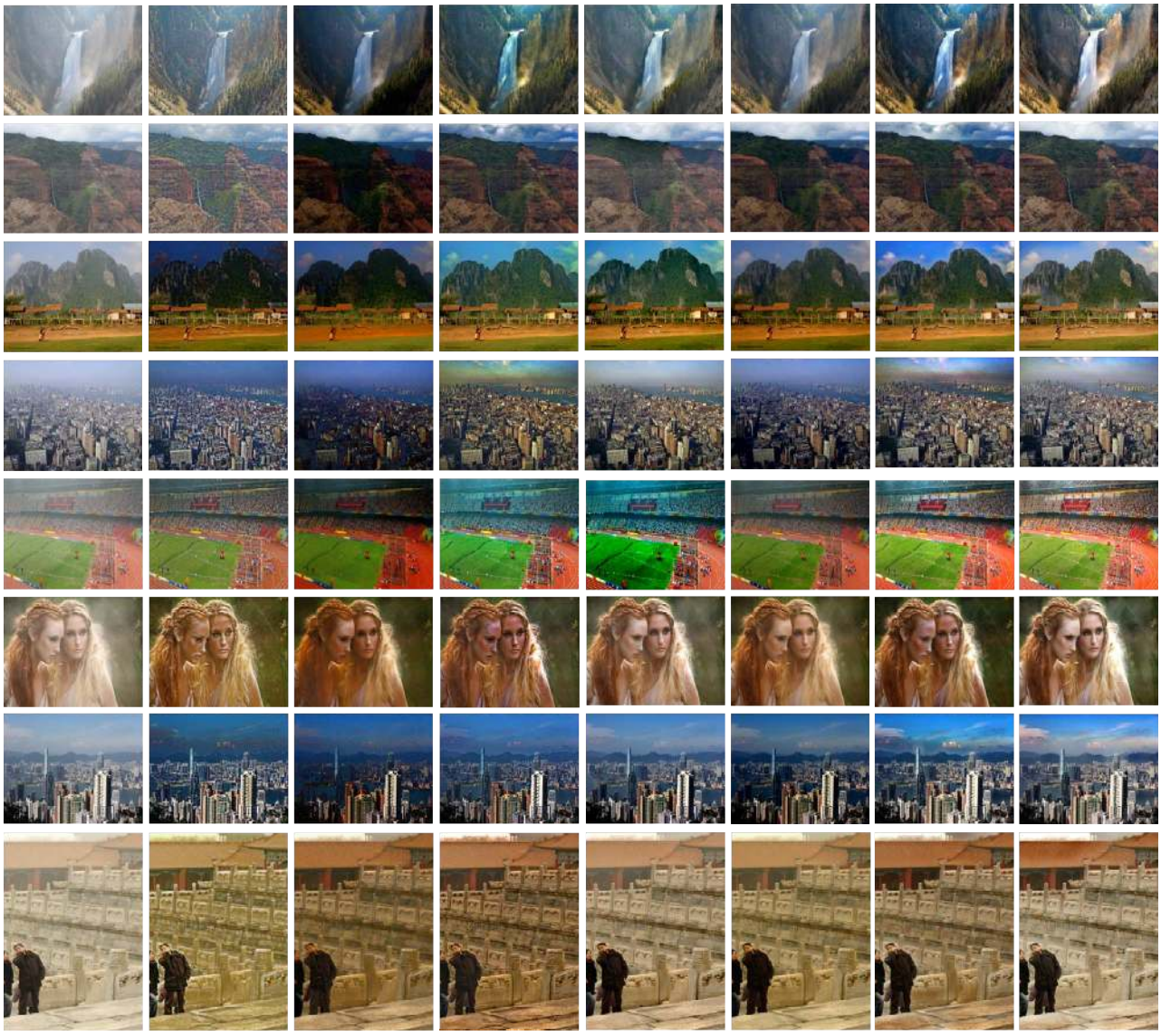

Figure 8: Comparison of dehazing results of state-of-the-art methods and our proposed method.

2nd(canyon), 6th (girls), 7th(city), and 8th rows (marble)).

In Fig. 9, we amplify the scenarios which contain the white, bright, and sky scenes. One can see that, when using the original DCP with fixed patch size, the color distortion is severe (see the red bounding boxes in the 2nd and 4th columns). However, with the use of the proposed patch map, the color distortion problems in these scenarios can be well avoided (see the blue bounding boxes in the 3rd and 4th columns). One can notice that the image presented in the 3th row is the picture which is used to demonstrate the limitation of the DCP in [4]. The reasons why our proposed method can solve the color distortion problem is that the PMS-Net can select the proper patch size for each pixel in the haze removal process. More specifically, in white or bright part, the patch map will be bigger in order to make the dark channel be near to zero (see the pictures in 5th column).

With this mechanism, the transmission map in the white and bright scenes may be higher comparing to original DCP method since the estimation of the transmission map in (5) can be applied without the error caused from the nonzero value of the dark channel.

4.4. Ablation Study

In this subsection, to demonstrate the improvement of using the proposed Multiscale U-module with the pyramid style in our PMS-Net, we perform the ablation study. This

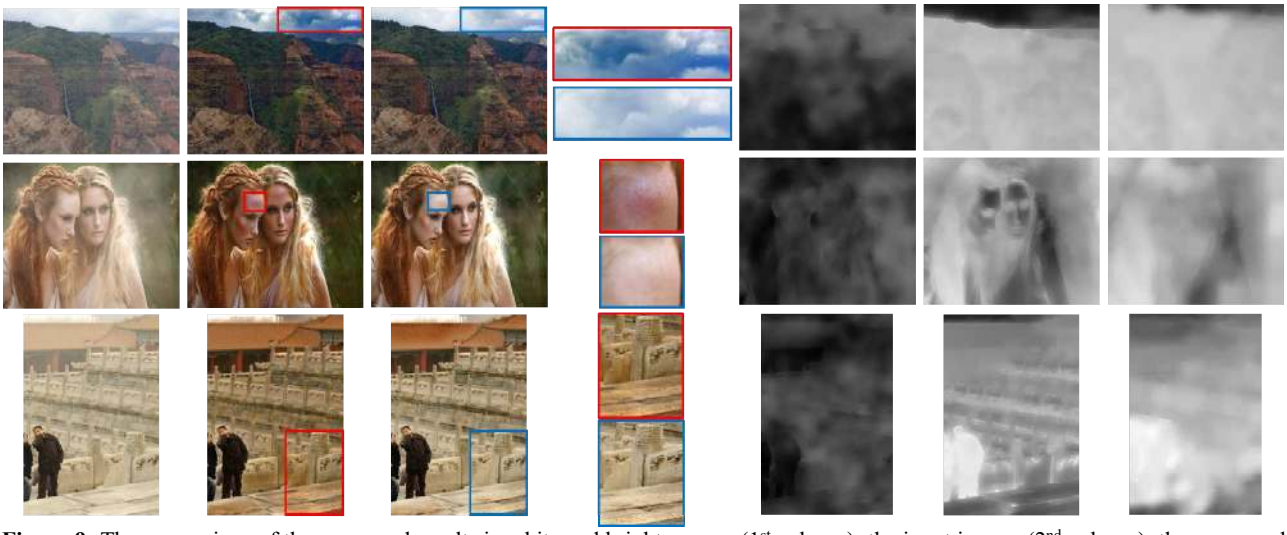

Figure 9: The comparison of the recovered results in white and bright scenes. (1st column): the input image; (2nd column): the recovered results by the conventional fixed patch size DCP; (3rd column): the recovered results by our proposed method; (4th column): the amplification of the white or bright portion in the 2nd and the 3rd columns; (5th column): the patch map; (6th and 7th columns): the transmission maps estimated by the DCP and our proposed method, respectively.

experiment includes five modules: 1) The PMS-Net without the Multiscale U-module and the pyramid style (**Module A**); 2) The PMS-Net with Multiscale U-module but without pyramid style (**Module B**); 3) The proposed algorithm using the Multiscale U-module with the pyramid style (**Module C**). We combine both Test A and Test B as one dataset in this experiment and apply the MSE for evaluation.

The results are shown in Table 3. The results show that, when we apply the multiscale U-module, comparing to Module A, the MSE be reduced by **8.7%**. Therefore, the proposed Multiscale U-module can enhance the accuracy of the patch map prediction effectively. Moreover, in our proposed Multiscale U-module, we perform the pyramid style in our network. One can notice that this architecture can not only improve 8.6% accuracy of the network but also decrease 30% of the parameters.

5. Conclusion and Analysis

In this paper, we demonstrate a novel haze removal algorithm by introducing a new feature-patch map. First, we investigate the reasons that limit the quality of the dehazed images when applying the conventional DCP based method. We find that the bad performances in white and bright scenes are due to the fixed patch size. Then, we notice that, after selecting the patch size properly and adaptively for each pixel, the recovered images can have outstanding performance comparing to other methods. Therefore, we define the patch map, and design the patch map selection network (PMS-Net) to estimate the proper patch size. In the design of the PMS-Net, we proposed the Multiscale U-module architecture, which consists of the Multiscale-W-ResBlocks and the Multi-Deconv blocks, to improve the performance. Moreover, in the design of the Multiscale U-module, we adopt the pyramid style to enhance the performance. With the patch map, a more accurate transmission map and a high-quality reconstructed results can be achieved. Furthermore, the bad performance in white and bright scenes can be well addressed by the patch map.

In experimental results, both qualitative evaluations and visual results show that our proposed method have better performance than existing methods. Moreover, with the ablation study, the Multiscale U-module with the pyramid style show that it can enhance the performance of the PMS-Net effectively.

Acknowledgments This work was supported by the Ministry of Science and Technology of Taiwan under grant MOST 105-2221-E-002-120-MY3.

References

[1] S. G. Narasimhan and S. K. Nayar. Chromatic framework for vision in bad weather. In *CVPR*, 2000.

[2] J.-P. Tarel and N. Hautiere. Fast visibility restoration from a single color or gray level image. In *CVPR, 2009*.

[3] R. Tan. Visibility in bad weather from a single image. In *CVPR*, 2008.

[4] K. He, J. Sun, and X. Tang. Single image haze removal using dark channel prior. In *CVPR*, 2009.

[5] R. Fattal. Single image dehazing. *ACM Trans. Graph*., vol. 27(3):72, 2008.

[6] R. Fattal. Dehazing using color-lines. *ACM Trans. Graph*., 34(1):13, 2014

[7] C. O. Ancuti, C. Ancuti, C. Hermans, and P. Bekaert. A fast semi-inverse approach to detect and remove the haze from a single image. In *ACCV,* 2011.

[8] C. O. Ancuti, C. Ancuti, and P. Bekaert. Effective single image dehazing by fusion. In *ICIP*, 2010.

[9] C. O. Ancuti and C. Ancuti. Single image dehazing by multiscale fusion. *IEEE Trans. on Image Processing*, 22(8):3271–3282, 2013

[10] Q. Zhu, J. Mai, and L. Shao. A fast single image haze removal algorithm using color attenuation prior. *IEEE Trans. Image Processing*, 24(11):3522–3533, 2015.

[11] G. Meng, Y. Wang, J. Duan, S. Xiang, and C. Pan. Efficient image dehazing with boundary constraint and contextual regularization. In *ICCV*, 2013.

[12] D. Berman, T. Treibitz, and S. Avidan. Non-local image dehazing. In *CVPR*, 2016.

[13] C. Chen, M. N. Do, and J. Wang. Robust Image and Video Dehazing with Visual Artifact Suppression via Gradient Residual Minimization. In *ECCV 2016*.

[14] K. Tang, J. Yang, and J. Wang. Investigating haze-relevant features in a learning framework for image dehazing. In *CVPR*, 2014.

[15] B. Cai, X. Xu, K. Jia, C. Qing, and D. Tao. Dehazenet: An end-to-end system for single image haze removal. *TIP*, 25(11):5187–5198, 2016.

[16] W. Ren, S. Liu, H. Zhang, J. Pan, X. Cao, and M.-H. Yang. Single image dehazing via multi-scale convolutional neural networks. In *ECCV*, 2016.

[17] B. Li, X. Peng, Z. Wang, J. Xu, and D. Feng. Aod-net: All in-one dehazing network. In *ICCV*, 2017.

[18] Y. Huang, Y Wang, and Z. Su. Single Image Dehazing Via a Joint Deep Modeling. In *ICIP*, 2018.

[19] G. Kim, S. Ha, and J. Kwon. Adaptive Patch Based Convolutional Neural Network for Robust Dehazing. In *ICIP,* 2018.

[20] D. Yang and J. Sun. Proximal dehaze-net: A prior learning-based deep network for single image dehazing, In *ECCV*, 2018.

[21] H. Zhang and V. M. Patel. Densely connected pyramid dehazing network. In *CVPR*, 2018.

[22] R. Li, J. Pan, Z. Li, and J. Tang. Single image dehazing via conditional generative adversarial network. In *CVPR*, 2018.

[23] D. Park, D. K. Han and H. Ko. Nighttime image dehazing with local atmospheric light and weighted entropy. In *ICIP,* 2016.

[24] Y. Li, R. T. Tan, and M. S. Brown. Nighttime haze removal with glow and multiple light colors. In *ICIP*, 2015.

[25] J. Zhang, Y. Cao, and Z. Wang. Nighttime haze removal based on a new imaging model. In *ICIP*, 2014

[26] C. Ancuti, C. O. Ancuti, A.C. Bovik, and Christophe De Vleeschouwer. Night time dehazing by fusion. In *ICIP*, 2014.

[27] J. Zhang, Y. Cao, S. Fang, Y. Kang, and C. W. Chen. Fast haze removal for nighttime image using maximum reflectance prior. In *CVPR*, 2017.

[28] W. T. Chen, S. Y. Yuan, G. C. Tsai, H. C. Wang, and S. Y. Kuo. Color channel-based smoke removal algorithm using machine learning for static images. In *ICIP*, 2018.

[29] L. Breiman. Random forests. *Mach. Learn*., 45(1), 2001

[30] B. Li, W. Ren, D. Fu, D. Tao, D. Feng, W. Zeng, and Z. Wang. Reside: A benchmark for single image dehazing. *arXiv preprint arXiv*:1712.04143, 2017.

[31] S. Zagoruyko and N. Komodakis, "Wide residual networks," *arXiv preprint arXiv*:1605.07146, 2016.

[32] K. He, X. Zhang, S. Ren, and J. Sun. Deep residual learning for image recognition. In *Proc. CVPR*, 2016.

[33] H. Noh, S. Hong, and B. Han. Learning deconvolution network for semantic segmentation. In *ICCV*, 2015.

[34] C. Peng, X. Zhang, G. Yu, G. Luo, and J. Sun. Large kernel matters improve semantic segmentation by global convolutional network. In *CVPR*, 2017

[35] D. Liu, D. Zhang, S. Liu, Y. Song, H. Jia, D. Feng, Y. Xia and W. Cai. Densely Connected Large Kernel Convolutional Network for Semantic Membrane Segmentation in Microscopy Images. In *ICIP*, 2018

[36] G. Huang, Z. Liu, K. Q. Weinberger, and L. Maaten. Densely connected convolutional networks. In *CVPR*, 2017.

[37] N. Silberman, D. Hoiem, P. Kohli, and R. Fergus. Indoor segmentation and support inference from rgbd images. In *ECCV*, 2012.

[38] D. Kingma and J. Ba. Adam: A method for stochastic optimization. In *ICLR*, 2015.

[39] L. K. Choi, J. You, and A. C. Bovik. Referenceless prediction of perceptual fog density and perceptual image defogging. *TIP*, 24(11):3888– 3901, 2015.

[40] L. K. Choi, J. You, and A. C. Bovik. Referenceless perceptual image defogging. In *SSIAI*, 2014.

[41] L. K. Choi, J. You, and A. C. Bovik. DEFADE Software Release;http://live.ece.utexas.edu/research/fog/DEFADE_release.zip, 2015.

[42] C. Szegedy, S. Ioffe, and V. Vanhoucke. Inception-v4, inception-resnet and the impact of residual connections on learning. In ICLR Workshop, 2016.